



OPEN

Microyielding of Core-Shell Crystal Dendrites in a Bulk-metallic-glass Matrix Composite

SUBJECT AREAS:
METALS AND ALLOYS
MECHANICAL PROPERTIESReceived
16 December 2013Accepted
20 February 2014Published
18 March 2014Correspondence and
requests for materials
should be addressed to
E-W.H. (EwenHuang.
NCU@gmail.com)E-Wen Huang¹, Junwei Qiao², Bartłomiej Winiarski^{3,4}, Wen-Jay Lee⁵, Mario Scheel⁶, Chih-Pin Chuang⁷, Peter K. Liaw⁷, Yu-Chieh Lo⁸, Yong Zhang⁹ & Marco Di Michiel⁶

¹Department of Chemical and Materials Engineering and Center for Neutron Beam Applications, National Central University, Jhongli, 32001, Taiwan (R.O.C.), ²Laboratory of Applied Physics and Mechanics of Advanced Materials, College of Materials Science and Engineering, Taiyuan University of Technology, Taiyuan 030024, China, ³Manchester X-ray Imaging Facility, School of Materials, University of Manchester, Manchester, M13 9PL, United Kingdom, ⁴National Physical Laboratory, Materials Division, London, M1 7HS, United Kingdom, ⁵National Center for High-Performance Computing, No. 22, Keyuan Rd., Central Taiwan Science Park, Taichung 40763, Taiwan (R.O.C.), ⁶European Synchrotron Radiation Facility Beamline ID15A, Grenoble, France, ⁷Department of Materials Science and Engineering, University of Tennessee, Knoxville TN 37996-2200, USA, ⁸Department of Nuclear Science and Engineering, Massachusetts Institute of Technology, 77 Massachusetts Avenue, 24-107 Cambridge, MA 02139, ⁹State Key Laboratory for Advanced Metals and Materials, University of Science and Technology, Beijing, 30 Xueyuan Road, Haidian District, Beijing 100083, China.

In-situ synchrotron x-ray experiments have been used to follow the evolution of the diffraction peaks for crystalline dendrites embedded in a bulk metallic glass matrix subjected to a compressive loading-unloading cycle. We observe irreversible diffraction-peak splitting even though the load does not go beyond half of the bulk yield strength. The chemical analysis coupled with the transmission electron microscopy mapping suggests that the observed peak splitting originates from the chemical heterogeneity between the core (major peak) and the stiffer shell (minor peak) of the dendrites. A molecular dynamics model has been developed to compare the *hkl*-dependent microyielding of the bulk metallic-glass matrix composite. The complementary diffraction measurements and the simulation results suggest that the interface, as Maxwell damper, between the amorphous matrix and the (211) crystalline planes relax under prolonged load that causes a delay in the reload curve which ultimately catches up with the original path.

Bulk metallic glasses (BMGs) are renowned for being very strong but also very brittle¹ because the extent of plastic deformation is limited by localized shear banding that leads to softening and catastrophic failure. By contrast, crystalline phases can accommodate plastic flow by dislocations², nano twins³, phase transformation^{4,5} and so on⁶, thereby distributing deformation so as not to form localized shear bands. Xia and Wang⁷ modelled the toughening effect of incorporating a ductile phase within a hard matrix. Along these lines crystalline phases have been added to brittle amorphous matrices to form BMG matrix composites (BMGMCs)⁸. Recent advances in BMGMCs^{4,5,9–18} show significant improvements in ductility, while retaining the characteristic strength of the parent BMGs. The homogeneity of plastic deformation introduced by a ductile phase is critical in imparting ductility and can be controlled by adding different types of reinforcements. Wang¹⁹ summarizes the roles of minor additions in the fabrication and modification of BMGs. In this vein, Abdeljawad and Haataja's simulations predict an inverse relationship between the size of crystalline particles and the ductility of the BMGMC⁹. Hofmann *et al.*²⁰ and Demetriou *et al.*²¹ experimentally confirm the importance of microstructural refinement as a means of toughening the BMGMC.

To date, the proposed micromechanisms for the plastic deformation of BMGMCs have been based on *ex-situ* observations. However, *in-situ* experiments can reveal the complementary real-time interactions between the amorphous matrix and the included crystalline phase. Ott *et al.*²² have measured the evolution of lattice-strain for crystalline Ta particles embedded in a metallic matrix by diffraction peak analysis using *in-situ* synchrotron X-ray diffraction, while ZrC crystal particles embedded in a BMG¹³ have been similarly studied. Meanwhile, Clausen *et al.* applied both Rietveld²³ and single-peak fitting²⁴ methods to study the diffraction profiles for the crystalline phase of a BMGMC. However, as mentioned by Furukawa and Tanaka²⁵, deformation may be inhomogeneous. In an attempt to study the spatial-temporal evolution of deformation, we have performed an *in-situ* compression



experiment combining ultrahigh spatial resolution hard x-ray imaging (200nm resolution) with x-ray diffraction at the European Synchrotron Radiation Facility (ESRF). This arrangement has enabled us to determine the ensemble-averaged crystalline phase response of the BMGMC while imaging the local arrangement by tomography. A complementary examination of the chemical-distribution coupled with electron microscopy was undertaken to identify microstructural effects on the diffraction profiles. To interpret the ensemble-averaged diffraction results, we have built a molecular dynamics simulation model to examine the behavior of the amorphous matrix/dendrite interface.

Results

The BMG/dendrite composite has a composition of $Zr_{58.5}Ti_{14.3}Nb_{5.2}Cu_{6.1}Ni_{4.9}Be_{11.0}$ in atomic percent (at. %) prepared by arc-melting a mixture of Zr, Ti, Nb, Cu, Ni, and Be with purity higher than 99.9% (weight percent) under an argon atmosphere²⁶. This BMGMC system is known for its good ductility¹⁰. A dog-bone-shape specimen was prepared for the *in-situ* compression experiment, as shown in the Figure S1. The sample was compressed by a small load rig accommodated on the beam line using the setup shown schematically in Figure S2.

The loads at which diffraction profiles were collected are marked in Figure 1(a) relative to the stress-strain curve²⁶ for an identical sample. It is evident that the load attained (1,000 MPa) is well within the engineering elastic limit. The sample was then almost completely unloaded to Pt 3, retaining a small force (about 20 N) to hold the specimen in the load rig. The (110), (200), and (211) diffraction planes confirm the body-centered-cubic (BCC) crystal structure of the dendrites²⁶. The evolution of the diffraction-profile measured for planes normal to the loading direction is shown in Figure 1(b–e). It is clear that upon compression, the original (110) peak splits into two overlapping peaks (labelled ‘m’ and ‘M’). Upon unloading, the split peaks change in intensity, but do not collapse back into a single peak. Similar peak splitting occurs for the (200) and (211) peaks too as

shown in Figure S3. To resolve these overlapping diffraction peaks, a double-peak fitting method has been applied which differs from other refinement methods applied to the *in-situ* diffraction experiments on BMGMCs^{13,22–24}. The broadening of the diffraction peaks will be referred to as the plastically induced strain²⁷ of the crystalline dendrites.

During the loading (Pt 1 → Pt 2) and unloading (Pt 2 → Pt 3) the diffraction rings corresponding to the crystalline dendrites were repeatedly collected and the corresponding evolutions in lattice strain for the major (M) and minor (m) peaks are shown in Figures 2(a), 2(b), and 2(c) for (110), (200), and (211) respectively. The corresponding changes in peak widths are presented in Figures 2(d), 2(e), and 2(f), accordingly.

In the Figures 2(a)–(c), the behaviors of the major and minor peaks are quite different. During compressive loading both peaks shift in a compressive sense, but the major peak shifts to a much higher degree. In fact both the (200) and (211) minor peaks appear to shift in a tensile sense until -100 MPa is exceeded, although it should be noted that it is very difficult to distinguish the minor peak at these low loads. It should be noted that the compressive load was held at a stress of -800 MPa for the (hours-long) tomography experiment. This may explain the relaxation of the *hkl*-dependent lattice strain and peak width between finishing the loading curve and starting the unloading one. Perhaps as a consequence of the prolonged hold time, upon unloading, none of the 3 major peaks retrace the original loading paths, varying little until the load has fallen below -500 MPa. Interestingly, the monolithic beta-crystalline phase embedded in an BMGMC system having a similar chemical composition to ours studied by Clausen *et al.*²⁴ has a yield stress of -610 MPa. However, in contrast to the observations by Clausen *et al.*, here the major peaks return to the original loading path upon unloading below -500 MPa.

Considering the peak width changes in Figures 2(d)–(f), initially the major peak narrows while the minor peak broadens until -200 MPa is exceeded after which both peaks plateau before both

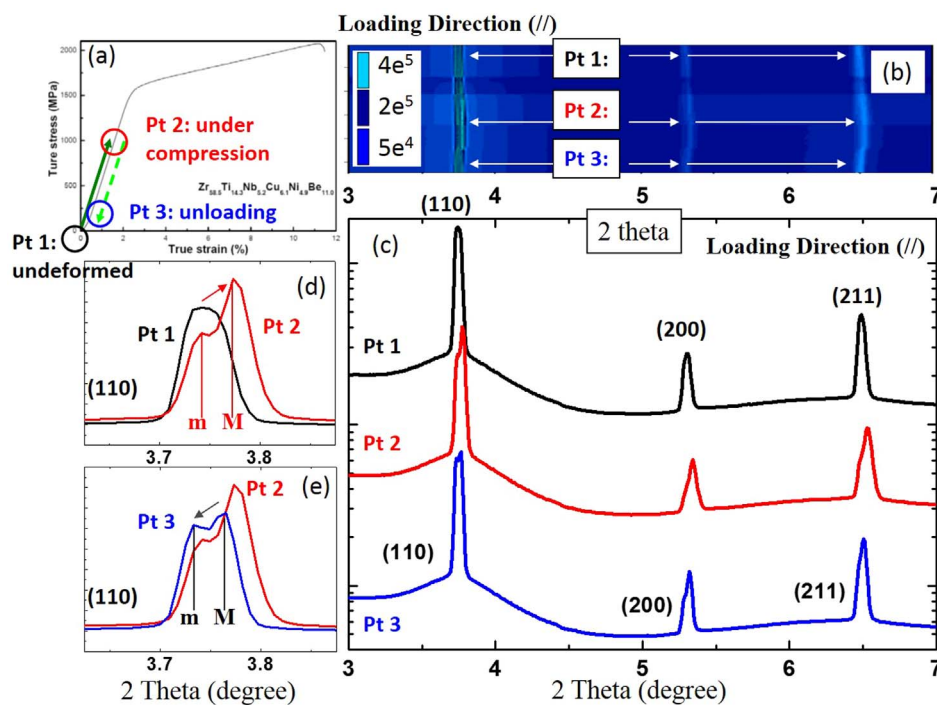


Figure 1 | (a) The undeformed (Pt 1), the compressed (Pt 2), and the unloaded states (Pt 3) at which the diffraction measurements were made alongside the stress-strain compression curve. (b) The evolution (shown vertically) of the diffraction profile corresponding to strains in the loading direction upon compression and unloading. (c) The corresponding diffraction line profiles for Pt 1, Pt 2, and Pt 3. (d) A comparison of the (110) peak before (black) and during (red) compression with the split peaks labelled “M” and “m”. (e) The retention of the peak splitting upon unloading.

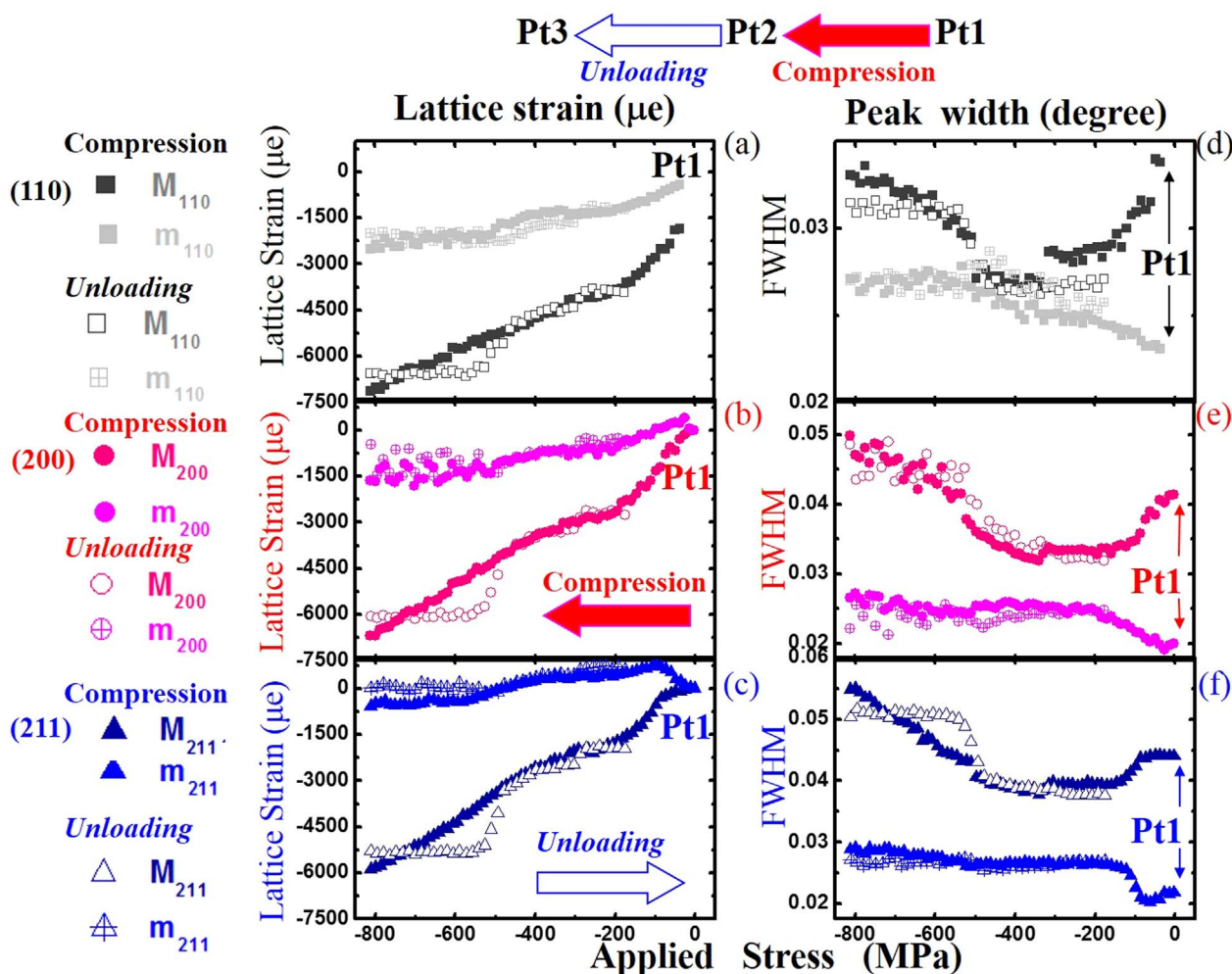


Figure 2 | Diffraction peak evolution (expressed in lattice strain) for the major peak (M) and the minor peak (m) for loading (filled symbols) and unloading (open symbols) for (a) (110), (b) (200), and (c) (211) and the corresponding changes in peak-widths for (d) (110), (e) (200), and (f) (211).

broaden, the major peak at the faster rate. As seen for the peak shifts, upon unloading there is some evidence that the widths are insensitive to unloading at first (this is most evident for the (211) peak) before retracing their loading paths below -500 MPa.

The most significant difference between the current results and previous *in-situ* synchrotron x-ray²² and neutron²⁴ diffraction results is the peak splitting. This suggests two distinct regions within the dendrites that respond differently to the applied stress. Recently, experimental results have suggested that even within a disordered bulk metallic glass, there might be two different regions showing distinct behaviors. Du *et al.* reported the possibility of two glassy phases for the Zr-Cu-Ni-Al system²⁸. Dmowski *et al.* showed 75% of the Zr-based BMG an elastic response to loading while 25% behaved inelastically²⁹. Ichitsubo *et al.*'s ultrasonic annealing³⁰ and Ohnuma's x-ray diffraction results³¹ also point to the presence of a strongly-bonded region (SBR) and a weakly-bonded region (WBR) in a Pd-based BMG and ferromagnetic-based amorphous ribbons, respectively. Along the same lines the quasi-static compression-unloading experiments of Huo *et al.* revealed a mechanical hysteresis stress-strain loop¹⁴. Further, Wang *et al.* describe such a hysteresis loop with a three-parameter model containing an elastic matrix, a flow unit, and the shell of a flow unit³².

Consequently a hypothetical "core-shell composite" model is proposed to describe our major and minor peaks. Our model is based on the interface depicted by Kelton and Greer³³ and Pieter Rein ten Wolde *et al.*³⁴ We propose that our major and minor peaks correspond to the core and shell/boundary regions of the dendrites,

respectively. This is analogous to the hard/soft models described by Eshelby's method to describe the internal strains of metal matrix composites³⁵.

To examine the grounds for this hypothesis, chemical mapping and electron microscopy was undertaken. In each case the spatial resolution was around 20 nm by 20 nm. The results are shown in Figure 3 for a representative dendrite/BMG interface which appears to show a transition region. The chemical compositions for the crystalline core and the amorphous regions in Figure 3 agree with those of Kühn *et al.*³⁶ However, the gradation in the boundary region is reported for the first time for this system. Similar chemical heterogeneity near the interface has also been seen previously in a brass-reinforced $\text{Ni}_{59}\text{Zr}_{20}\text{Ti}_{16}\text{Si}_2\text{Sn}_3$ bulk metallic glass composite³⁷. Consequently we conclude that the distinct splitting into major and minor peaks arises from the differences between the chemical compositions of the core and shell regions of the dendrites.

Discussion

To identify which regions of the dendrites correspond to the major and minor diffraction peaks, we compare the chemically dependent modulus and lattice parameters. The TEM diffraction spots for the shell and core regions suggest that the major peak at the higher scattering angle (2θ) corresponds to the smaller lattice parameter found at the core and the minor peak at the lower angle is associated with the shell (boundary region). The lattice modulus of the dendrite cores is inferred from Figure 2 to be lower than that of the boundary

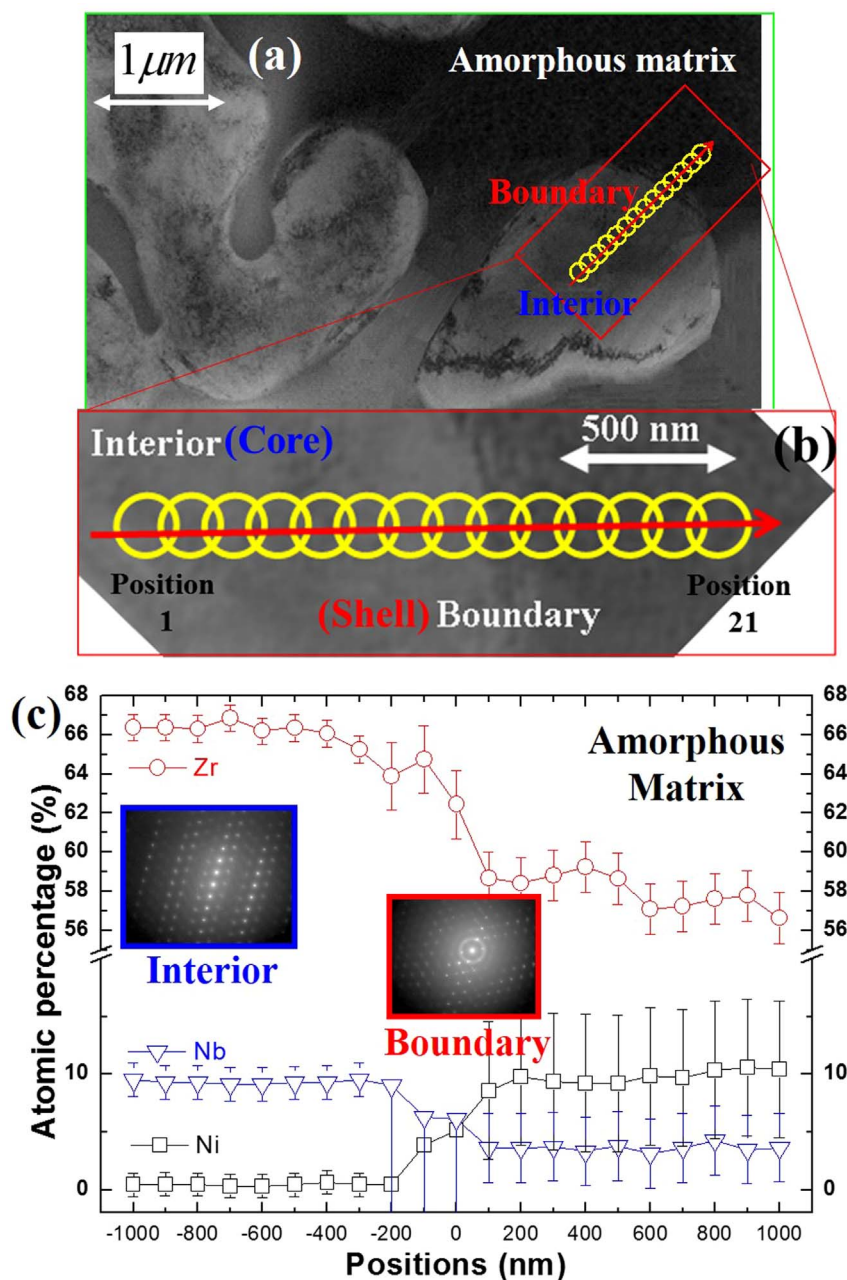


Figure 3 | Transmission electron microscopy and the associated chemical-profiling. (a) TEM micrograph showing the phase boundaries and the line for chemical profiling (b) Line scan from the interior (most left) of the dendrite to the amorphous matrix (most right). (c) The chemical distribution of the major components (Ni, Nb and Zr) of the BMGMC along the scan line alongside corresponding TEM diffraction patterns.

regions. This stiffer “Shell” and softer “Core” deduction agrees with BMG–brass interfaces results³⁷. As discussed above, the local structure plays an important role during the deformation. For example, Jiang *et al.* reported spatiotemporally inhomogeneous deformation³⁸. The simulations^{39,40,11}, including Cleri’s “Core-Shell” simulations⁴¹, as well as the experiments of Jang *et al.*⁴², have helped elucidate the cooperative activation of lattice dislocations on the glass-crystal boundaries. Following on from this literature, we have developed a model to examine the role of the interface in the light of our measured lattice-strain changes. A Large-scale Atomic/Molecular Massively Parallel Simulator (LAMMPS)⁴³ code has been used (see Methods for details) to simulate the amorphous matrix/dendrite boundary region in order to simulate the evolution of the lattice-spacing for the shell region (minor peak). The strain response of the (110) and (211) lattice planes under compression (Figures 2(a) and

2(c)) are selected for comparison because the $\{110\}\langle 111\rangle$ and $\{211\}\langle 111\rangle$ slip systems are expected both theoretically⁴⁴ and experimentally⁴⁵ to have the minimum tensile and shear strengths. However, $\{110\}\langle 111\rangle$ shear differs from $\{211\}\langle 111\rangle$ shear in the lattice relaxation behavior⁴⁴. The relaxation returns the deformed structure to the BCC structure at a specific strain level through a saddle-point structure⁴⁴.

The measured (110) and (211) lattice strain responses for the minor (shell) peaks are reproduced in Figures 4(a) and 4(b), respectively. In Figure 4(a), within -300 MPa to -500 MPa, the (110) lattice strain is more compressive subjected to unloading. Beyond -500 MPa, there is no clear difference. On the other hand, in Figure 4(b), there is significant relaxation after the holding from -800 MPa to -500 MPa for the (211) lattice strain where is less compressive subjected to unloading.

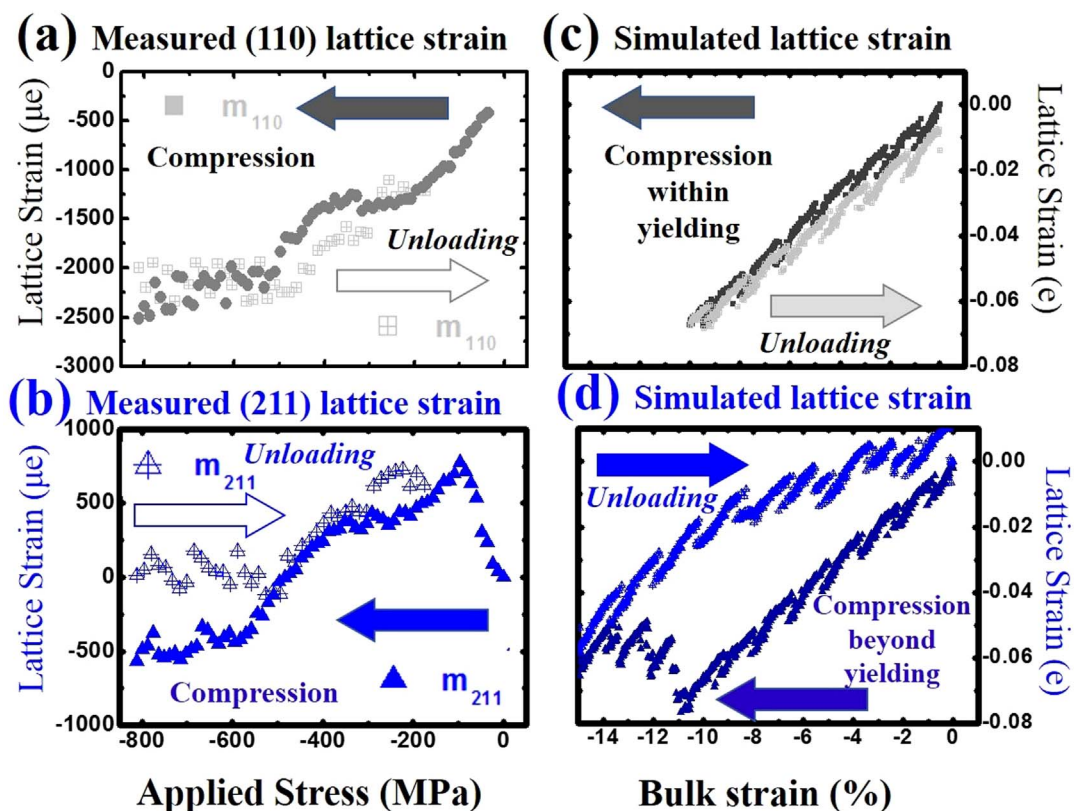


Figure 4 | The measured loading-unloading responses of (a) the (110) and (b) the (211) shell (minor) diffraction peaks for lattice strain. The simulated compression-unloading loop of the lattice strain experienced stress: (c) before and (d) beyond yielding, respectively.

The simulated lattice-strain evolution within yielding and beyond yielding are shown in Figures 4(c) and 4(d), respectively. Upon compression, both simulated lattice strain also show nonlinear responses. In Figure 4(c), the compressive loading-unloading cycle is within yielding, lattice strain is more compressive subjected to unloading and there is no clear difference. However, in Figure 4(d), while unloading, unlike the measured relaxation phenomena subjected to the holding, we did not simulate the holding. Although at the end of the cycle, the simulated lattice strain almost come back to that of the beginning, there is clear hysteresis response and lattice strain is less compressive subjected to unloading. The differences between the simulated lattice-strain responses might reflect the different saddle-point structures between $\{110\}\langle 111\rangle$ and $\{211\}\langle 111\rangle$ shear paths⁴⁴. Moreover, the (211) lattice-strain evolution shows the features of microstructure relaxation⁴⁶. The effect of our simplified deformation-accommodation picture of the interface agrees with the phenomena of Xu and Lu's interface model⁴⁷. The mechanisms rely on the ductile particles limiting the shear extension and/or retarding the shear-band propagation via forming a "plastic zone" in their constrained amorphous matrix. Wang *et al.*'s⁴⁸ simulation suggests the amorphous-crystal interfaces exhibit unique inelastic shear (slip) transfer characteristics where the glassy layers can act as high-capacity sinks enabling absorption of deformation. Hence, the observed simulated and measured lattice-strain loop might originate from the deformation of metallic glasses, which are then accommodated by the crystalline phase⁴⁹.

In summary, our experiments directly observe the composite behavior of the crystalline dendrites in the BMGMC. Our work has reported distinct splitting for the first time. This suggests that the particles have a characteristic core-shell character. The major (core) and minor (shell) peak shifts and peak broadenings of the crystalline dendrites indicate that strain heterogeneity relaxes. Different lattice-

strain behaviors of the interfaces show the hkl -dependent relaxation near the interface, as Maxwell damper. The tangled boundaries and the rearranged interiors accommodate the plasticity over the hold time when the tomography was collected. While unloading to smaller compression, the reversible peak widths and lattice strains of all hkl planes suggest statistically-resilient arrangements.

Methods

In-situ diffraction experiments. The diffraction experiments sample a gauge volume of $120\ \mu\text{m} \times 120\ \mu\text{m}$ indicated by the red box of the Figure S1. In order to collect the sufficient transmitted diffraction signal, a compromise between the best energy for the X-ray lens arrangement on the beamline⁵⁰ and for the penetration through the relatively heavy atomic number of our sample is set at 46 keV. More specifically, to ensure sufficient penetration, the cross-section of the sample gauge was machined down to less than $500\ \mu\text{m}$, as shown in Figure S1. The evolution of the diffraction-peak profiles were measured during the deformation experiment and an area detector focusing on the horizontal (equatorial) and vertical (polar) arcs recorded the loading and transverse directional information simultaneously (Figure S2).

Molecular dynamics simulation. The calculations were performed on a range of massively parallel platforms. A model of half-dendrite, half-matrix and their interface was built around Cleri and Rosato's concept⁵¹. A box about $136\text{\AA} \times 68\text{\AA} \times 204\text{\AA}$ is developed to contain the systems, respectively. The periodic boundary conditions are applied in all three spatial directions. The embedded atom model (EAM) was used to describe the interaction between the atoms of the system in the MD simulation. Because our focus was on relationship between the crystalline, amorphous phases, and the interface, we have simplified the material to a binary-element system comprising 50% Zr and 50% Cu. The reason to select the Zr and Cu is based on their empirical formability of the amorphous phase reported elsewhere¹². The potential parameters are taken from Hao *et al.*⁵² An isothermal-isobaric ensemble is applied to define our experimental conditions at a fixed pressure P (1 atm), temperature T (300 K), and number of atoms N (more than 115,000) as an NPT ensemble. We also applied Nosé-Hoover thermostat and barostat in the current MD simulation. Velocity Verlet algorithm is employed to calculate the trajectories of the atoms. A time step of 2 fs was set for the time integration. Before the loading, a relaxation process of 10,000 steps was applied to eliminate the internal stresses. After relaxation, the model was subjected to a constant compression strain rate of $10^{10}\ \text{s}^{-1}$ in the loading direction.



1. Jang, D. C. & Greer, J. R. Transition from a strong-yet-brittle to a stronger-and-ductile state by size reduction of metallic glasses. *Nat. Mater.* **9**, 215–219 (2010).
2. Chen, M. W., Inoue, A., Zhang, W. & Sakurai, T. Extraordinary plasticity of ductile bulk metallic glasses. *Phys. Rev. Lett.* **96**, 245502 (2006).
3. Pauly, S., Gorantla, S., Wang, G., Kuhn, U. & Eckert, J. Transformation-mediated ductility in CuZr-based bulk metallic glasses. *Nat. Mater.* **9**, 473–477 (2010).
4. Oh, Y. S., Kim, C. P., Lee, S. & Kim, N. J. Microstructure and tensile properties of high-strength high-ductility Ti-based amorphous matrix composites containing ductile dendrites. *Acta Mater.* **59**, 7277–7286 (2011).
5. Mu, J. *et al.* In situ high-energy X-ray diffraction studies of deformation-induced phase transformation in Ti-based amorphous alloy composites containing ductile dendrites. *Acta Mater.* **61**, 5008–5017 (2013).
6. Cheng, J.-L., Chen, G., Liu, C.-T. & Li, Y. Innovative approach to the design of low-cost Zr-based BMG composites with good glass formation. *Sci. Rep.* **3**, (2013).
7. Xia, S. H. & Wang, J. T. A micromechanical model of toughening behavior in the dual-phase composite. *Int. J. Plast.* **26**, 1442–1460 (2010).
8. Hays, C. C., Kim, C. P. & Johnson, W. L. Microstructure controlled shear band pattern formation and enhanced plasticity of bulk metallic glasses containing in situ formed ductile phase dendrite dispersions. *Phys. Rev. Lett.* **84**, 2901–2904 (2000).
9. Abdeljawad, F. & Haataja, M. Continuum Modeling of Bulk Metallic Glasses and Composites. *Phys. Rev. Lett.* **105**, 125503 (2010).
10. Qiao, J. W. *et al.* Tensile deformation micromechanisms for bulk metallic glass matrix composites: From work-hardening to softening. *Acta Mater.* **59**, 4126–4137 (2011).
11. Zhou, H. F., Qu, S. X. & Yang, W. An atomistic investigation of structural evolution in metallic glass matrix composites. *Int. J. Plast.* **44**, 147–160 (2013).
12. Liu, M. C. *et al.* Assessing the interfacial strength of an amorphous-crystalline interface. *Acta Mater.* **61**, 3304–3313 (2013).
13. Suzuki, H. *et al.* Evaluation of compressive deformation behavior of Zr₅₅Al₁₀Ni₅Cu₃₀ bulk metallic glass containing ZrC particles by synchrotron X-ray diffraction. *Scripta Mater.* **66**, 801–804 (2012).
14. Huo, L. S. *et al.* The deformation units in metallic glasses revealed by stress-induced localized glass transition. *J. Appl. Phys.* **111** (2012).
15. Tian, L. *et al.* Approaching the ideal elastic limit of metallic glasses. *Nat Commun* **3**, 609 (2012).
16. Chou, H. S., Du, X. H., Lee, C. J. & Huang, J. C. Enhanced mechanical properties of multilayered micropillars of amorphous ZrCuTi and nanocrystalline Ta layers. *Intermetallics* **19**, 1047–1051 (2011).
17. Jang, J. S. C., Li, T. H., Jian, S. R., Huang, J. C. & Nieh, T. G. Effects of characteristics of Mo dispersions on the plasticity of Mg-based bulk metallic glass composites. *Intermetallics* **19**, 738–743 (2011).
18. Qiao, J. W. *et al.* A Tensile Deformation Model for In-situ Dendrite/Metallic Glass Matrix Composites. *Sci. Rep.* **3** (2013).
19. Wang, W. H. Roles of minor additions in formation and properties of bulk metallic glasses. *Prog. Mater. Sci.* **52**, 540–596 (2007).
20. Hofmann, D. C. *et al.* Designing metallic glass matrix composites with high toughness and tensile ductility. *Nature* **451**, 1085–1089 (2008).
21. Demetriou, M. D. *et al.* A damage-tolerant glass. *Nat. Mater.* **10**, 123–128 (2011).
22. Ott, R. T. *et al.* Micromechanics of deformation of metallic-glass-matrix composites from in situ synchrotron strain measurements and finite element modeling. *Acta Mater.* **53**, 1883–1893 (2005).
23. Clausen, B. *et al.* Compressive yielding of tungsten fiber reinforced bulk metallic glass composites. *Scripta Mater.* **49**, 123–128 (2003).
24. Clausen, B. *et al.* Compressive deformation of in situ formed bulk metallic glass composites. *Scripta Mater.* **54**, 343–347 (2006).
25. Furukawa, A. & Tanaka, H. Inhomogeneous flow and fracture of glassy materials. *Nat. Mater.* **8**, 601–609 (2009).
26. Qiao, J. W., Zhang, Y., Liaw, P. K. & Chen, G. L. Micromechanisms of plastic deformation of a dendrite/Zr-based bulk-metallic-glass composite. *Scripta Mater.* **61**, 1087–1090 (2009).
27. Barabash, R. *et al.* White microbeam diffraction from distorted crystals. *Appl. Phys. Lett.* **79**, 749–751 (2001).
28. Du, X. H. *et al.* Two-glassy-phase bulk metallic glass with remarkable plasticity. *Appl. Phys. Lett.* **91**, 131901–131903 (2007).
29. Dmowski, W. *et al.* Structural rejuvenation in a bulk metallic glass induced by severe plastic deformation. *Acta Mater.* **58**, 429–438 (2010).
30. Ichitsubo, T. *et al.* Microstructure of fragile metallic glasses inferred from ultrasound-accelerated crystallization in Pd-based metallic glasses. *Phys. Rev. Lett.* **95**, 245501 (2005).
31. Ohnuma, M. *et al.* Structural anisotropy of amorphous alloys with creep-induced magnetic anisotropy. *Acta Mater.* **60**, 1278–1286 (2012).
32. Wang, Z., Wen, P., Huo, L. S., Bai, H. Y. & Wang, W. H. Signature of viscous flow units in apparent elastic regime of metallic glasses. *Appl. Phys. Lett.* **101**, 121906–121904 (2012).
33. Kelton, K. & Greer, A. L. *Nucleation in Condensed Matter: Applications in Materials and Biology*. (Elsevier Science, 2010).
34. Wolde, P. R. t., Ruiz-Montero, M. J. & Frenkel, D. Numerical Evidence for bcc Ordering at the Surface of a Critical fcc Nucleus. *Phys. Rev. Lett.* **75**, 2714–2717 (1995).
35. Withers, P. J., Stobbs, W. M. & Pedersen, O. B. The application of the eshelby method of internal stress determination to short fibre metal matrix composites. *Acta Metall.* **37**, 3061–3084 (1989).
36. Kuhn, U., Eckert, J., Mattern, N. & Schultz, L. ZrNbCuNiAl bulk metallic glass matrix composites containing dendritic bcc phase precipitates. *Appl. Phys. Lett.* **80**, 2478–2480 (2002).
37. Wang, K. *et al.* Interface structure and properties of a brass-reinforced Ni₅₉Zr₂₀Ti₁₆Si₂Sn₃ bulk metallic glass composite. *Acta Mater.* **56**, 3077–3087 (2008).
38. Jiang, W. H. *et al.* Spatiotemporally inhomogeneous plastic flow of a bulk-metallic glass. *Int. J. Plast.* **24**, 1–16 (2008).
39. Fornell, J. *et al.* Yielding and intrinsic plasticity of Ti-Zr-Ni-Cu-Be bulk metallic glass. *Int. J. Plast.* **25**, 1540–1559 (2009).
40. Zhao, P. Y., Li, J. & Wang, Y. Z. Heterogeneously randomized STZ model of metallic glasses: Softening and extreme value statistics during deformation. *Int. J. Plast.* **40**, 1–22 (2013).
41. Cleri, F. A two-phase model of large-strain plasticity in covalent nanostructures. *Int. J. Plast.* **37**, 31–52 (2012).
42. Jang, D. C., Gross, C. T. & Greer, J. R. Effects of size on the strength and deformation mechanism in Zr-based metallic glasses. *Int. J. Plast.* **27**, 858–867 (2011).
43. Maillat, J. B., Lachet, V. & Coveney, P. V. Large scale molecular dynamics simulation of self-assembly processes in short and long chain cationic surfactants. *PCCP* **1**, 5277–5290 (1999).
44. Luo, W., Roundy, D., Cohen, M. L. & Morris, J. W. Jr. Ideal strength of bcc molybdenum and niobium. *Phys. Rev. B* **66**, 094110 (2002).
45. Kim, J.-Y., Jang, D. & Greer, J. R. Insight into the deformation behavior of niobium single crystals under uniaxial compression and tension at the nanoscale. *Scripta Mater.* **61**, 300–303 (2009).
46. Chen, K. & Schweizer, K. S. Microscopic constitutive equation theory for the nonlinear mechanical response of polymer glasses. *Macromolecules* **41**, 5908–5918 (2008).
47. Xu, Q. & Lu, Z. X. An elastic-plastic cohesive zone model for metal-ceramic interfaces at finite deformations. *Int. J. Plast.* **41**, 147–164 (2013).
48. Wang, Y., Li, J., Hamza, A. V. & Barbee, T. W. Ductile crystalline-amorphous nanolaminates. *PNAS* **104**, 11155–11160 (2007).
49. Ye, J. C., Lu, J., Liu, C. T., Wang, Q. & Yang, Y. Atomistic free-volume zones and inelastic deformation of metallic glasses. *Nat Mater* **9**, 619–623 (2010).
50. Marrow, T. J., Buffiere, J. Y., Withers, P. J., Johnson, G. & Engelberg, D. High resolution X-ray tomography of short fatigue crack nucleation in austempered ductile cast iron. *Int. J. Fatigue* **26**, 717–725 (2004).
51. Cleri, F. & Rosato, V. Tight-binding potentials for transition metals and alloys. *Phys. Rev. B* **48**, 22–33 (1993).
52. Hao, S. G., Wang, C. Z., Kramer, M. J. & Ho, K. M. Microscopic origin of slow dynamics at the good glass forming composition range in Zr_{1-x}Cu_x metallic liquids. *J. Appl. Phys.* **107**, 053511–053516 (2010).

Acknowledgments

All the authors sincerely thank Prof. Philip J. Withers' help and advice. EWH appreciates the support from National Science Council (NSC) Programs NSC101-2221-E-008-039-MY3 and NSC-102-3113-P-007-014. Three graduate students under EWH's supervision gave particular help: Mr. Jer-Yi Liao's TEM and EDX work; Yu-Lih Huang's simulation, and Mr. Chung-Kai Chang's tomography analysis. We are grateful to the National Center for High-performance Computing for computer time and facilities. JWQ would like to acknowledge the financial support of National Natural Science Foundation of China (No.51101110 and No.51371122) and Research Project Supported by Shanxi Scholarship Council of China (No.2012-032). BW would like to acknowledge the EPSRC for funding through grant EP/F028431/1 and EP/I02249X/1. PKL and his group members very much appreciate the financial support from the US National Science Foundation (DMR-0909037, CMMI-0900271, and CMMI-1100080), the Department of Energy (DOE), Office of Nuclear Energy's Nuclear Energy University Program (NEUP) 00119262, the DOE, Office of Fossil Energy, National Energy Technology Laboratory (DE-FE-0008855 and DE-FE-0011194), and the Army Research Office (W911NF-13-1-0438), with C. Huber, C. V. Cooper, D. Finotello, A. Ardell, E. Taleff, V. Cedro, R. O. Jensen, L. Tan, S. Lesica, S. Markovich, and S. Mathaudhu as contract monitors.

Author contributions

E.W.H., J.W.Q. and B.W. designed the experiments. J.W.Q., Y.Z., P.K.L. and B.W. prepared the samples. E.W.H., B.W., C.P.C., M.S. and M.D.M. carried out the experiments. W.J.L., E.W.H. and Y.C.L. conducted the simulation. E.W.H. analyzed the data and wrote the paper.

Additional information

Supplementary information accompanies this paper at <http://www.nature.com/scientificreports>

Competing financial interests: The authors declare no competing financial interests.



How to cite this article: Huang, E.-W. *et al.* Microyielding of Core-Shell Crystal Dendrites in a Bulk-metallic-glass Matrix Composite. *Sci. Rep.* 4, 4394; DOI:10.1038/srep04394 (2014).



This work is licensed under a Creative Commons Attribution-NonCommercial-NoDerivs 3.0 Unported license. To view a copy of this license, visit <http://creativecommons.org/licenses/by-nc-nd/3.0>